Observation of spatial propagation of amyloid assembly from single nuclei

Tuomas P. J. Knowles[a,b], Duncan A. White[b], Adam R. Abate[a,1], Jeremy J. Agresti[a], Samuel I. A. Cohen[b], Ralph A. Sperling[a], Erwin J. De Genst[b], Christopher M. Dobson[b,2], and David A. Weitz[a,2]

[a]Department of Physics and School of Engineering and Applied Sciences, Harvard University, Cambridge, MA 02138; and [b]Department of Chemistry, University of Cambridge, Cambridge CB2 1EW, United Kingdom

The crucial early stages of amyloid growth, in which normally soluble proteins are converted into fibrillar nanostructures, are challenging to study using conventional techniques yet are critical to the protein aggregation phenomena implicated in many common pathologies. As with all nucleation and growth phenomena, it is difficult to track individual nuclei in traditional macroscopic experiments, which probe the overall temporal evolution of the sample, but do not yield detailed information on the primary nucleation step as they mix independent stochastic events into an ensemble measurement. To overcome this limitation, we have developed microdroplet assays enabling us to detect single primary nucleation events and to monitor their subsequent spatial as well as temporal evolution, both of which we find to be determined by secondary nucleation phenomena. By deforming the droplets to high aspect ratio, we visualize in real-time propagating waves of protein assembly emanating from discrete primary nucleation sites. We show that, in contrast to classical gelation phenomena, the primary nucleation step is characterized by a striking dependence on system size, and the filamentous protein self-assembly process involves a highly nonuniform spatial distribution of aggregates. These findings deviate markedly from the current picture of amyloid growth and uncover a general driving force, originating from confinement, which, together with biological quality control mechanisms, helps proteins remain soluble and therefore functional in nature.

microfluidics | reaction front | filamentous growth | insulin | protein misfolding

The conversion of proteins from their soluble native states into filamentous supramolecular amyloid assemblies is a generic type of behavior observed for a wide variety of protein molecules with very different primary and secondary structures (1–3). Moreover, this aggregation process is implicated as the key molecular event leading to pathological deposition of proteins in conditions such as Alzheimer's and Parkinson diseases, and type II diabetes (4–6). The traditional view of filamentous protein growth has emerged in large part from studies of the cytoskeletal proteins actin and tubulin and has led to a picture where each filament grows by elongation from a single independent primary nucleus (7). Recent evidence suggests, however, that amyloid growth is far more complex, apparently involving not only primary nucleation but different forms of secondary nucleation (8–11) that enable multiple fibrils to be generated from a single primary nucleation event; this mechanism is analogous to that originally discovered for sickle hemoglobin aggregation (12, 13).

To elucidate the fundamental mechanisms underlying amyloid formation, it is essential to understand the elusive early stages of this phenomenon; i.e., the initial primary nucleation events. It is not readily possible to isolate a single nucleus in a macroscopic sample but a particularly elegant method to overcome this limitation was pioneered by Turnbull to elucidate the solidification of metals, namely to use emulsions to restrict the spread of individual nucleation events (14). Although droplets have been used very successfully to investigate aspects of protein crystallization (15) and aggregation (16), their unique capabilities in addressing the challenge of monitoring single amyloid nucleation events and their spatial propagation have not until now been exploited.

Here we use microfluidic technology (17, 18) to segregate single nucleation sites into microdroplets. By developing methods and devices that allow a large ensemble of individual droplets to be stabilized during incubation, and then to be observed individually as a function of time in a stable manner, we are able to track the formation of single primary nuclei and their development into traveling waves that rapidly take over the entire droplet in which they form. We use nonspherical high aspect ratio droplets and observe that the reaction front driving amyloid conversion propagates as a wave along the long axis of the droplet. By varying the droplet size we show further that when the system size decreases beyond a critical volume there is a marked increase in the lag time prior to the observation of protein aggregation. This increased lag time under these microscopic conditions reflects a marked decrease in the primary nucleation rate resulting from increasing confinement and constitutes a fundamental physical mechanism that contributes to the kinetic stability of proteins. These experiments overcome a major limitation of bulk measurements, namely that secondary nucleation events obscure the primary nucleation processes; on the micron scale, however, we show that this limitation no longer exists and that it is possible to measure both primary and secondary events independently (i.e., to follow both the initial nucleation step and its subsequent propagation).

We use as an experimental system the hormone insulin, one of the first proteins to have been observed to undergo a fibrillar conversion in vitro (19), and a system widely used to explore the phenomenon of amyloid assembly (20–22). The aggregation of insulin is also of considerable practical significance in the context of moderating the stability of pharmaceutical preparations used in the treatment of diabetes (23). Insulin aggregation can also lead in vivo to injection amyloidosis (24), an example of a wider class of amyloid disorders (4, 5) that includes pathologies such as Alzheimer's disease and the prion conditions (25).

Results

To probe the growth of protein aggregates from single primary nucleation events, we have designed a microfluidic device, shown

schematically in Fig. 1*A*, which integrates a microdroplet maker (Fig. 1*B*) with a storage element (Fig. 1*C*), where droplets are deformed to generate the required high aspect ratios and arranged in arrays within the device for parallel measurements (26) (Movie S1). We encapsulate insulin molecules together with amyloidophilic fluorophores in aqueous droplets formed within an inert flurocarbon oil. To ensure the complete inertness of the droplet interface, we add surfactant molecules to the oil phase; these water-insoluble species localize at the oil/water interface and expose a protein-repelling polyethylene glycol layer to the aqueous phase (Fig. 1*A*) (16, 27). The droplets are formed at room temperature and incubated at 60 °C to initiate the aggregation process. Fluorescence images acquired at regular intervals enable us to follow the appearance of misfolded and aggregated species through the increase in thioflavin T fluorescence associated with the binding of the dye to amyloid structures (Fig. 1*D*). Recently, there has been much interest in developing amyloidophilic probes with an increased sensitivity and selectivity (28), and such molecules could be used in the future to provide further information during the aggregation reaction in microfluidic assays of the type that we describe in this paper.

The compartmentalization on the micron scale achieved in these experiments is crucial. It enables us to establish that the primary nucleation events we observe are discrete, thereby allowing us to follow both the temporal and spatial evolution of each individual event. Fluorescence microscopy reveals that primary nucleation eventually occurs in all droplets, and that for any given event the fluorescence spreads out from a single point. Initially, the amyloid configurations span the width of the droplet; thereupon the growth proceeds along the length of the droplet, eventually filling the entire volume with misfolded protein molecules, as shown by the time sequence for a single droplet in (Fig. 2*A* and Movies S2 and S3). The fluorescence intensity is distributed throughout the droplet, showing that no localization at the interface is occurring.

The linear geometry of our systems reveals a dramatic feature of amyloid conversion: It proceeds as a traveling wave propagating linearly in time from the primary nucleation site along the length of the droplet (Fig. 2 *A* and *B*, *Insert* and Movie S3). Furthermore, the system geometry allows the propagation velocity to be determined accurately (Fig. 2*B*); remarkably, it is constant in time $v_w = 70.9 \pm 9$ nm s^{-1}, in stark contrast to simple diffusive spreading that exhibits a square root time dependence.

Fig. 2. Propagation of amyloid growth within microdroplets. Single droplets are observed as a function of time: bright field microscopy (*A*, *Upper*) and fluorescence microscopy (*A*, *Lower*) images acquired at regular intervals during the incubation of a droplet. The widths of all the droplets analyzed here are 30 μm, and their heights are 25 μm leading to a constant Laplace pressure inside all the droplets independent of their length. (*B*, *Inset*) The integrated fluorescence intensity from the droplet as a function of time. In *B* is shown the velocity of the reaction front measured in two different drop geometries; blue lines denote velocity measurements in elongated droplets, green in corrugated droplets as shown in the insert and red for measurements in elongated droplets acquired for protein solutions purified by size exclusion chromatography (*Materials and Methods*). The gray lines are the corresponding results from the simulations in Fig. 3. (*C*) The width of the reaction front measured in the microdroplets (blue lines) and from the simulation in Fig. 3 (gray lines).

Fig. 1. Schema illustrating the design of the microfluidic device used in this study (*A*). A droplet maker (*B*) is coupled to a storage element (*C*) where elongated drops are incubated and can be monitored individually as a function of time. (*D*) Schema illustrating the encapsulation of protein molecules (blue spheres) and thioflavin T fluorophores (green spheres) into aqueous droplets stabilized by perfluorinated polyether-polyethyleneglycol (PFPE-PEG) block-copolymer surfactants. Misfolded proteins that assemble into cross-β structures can be detected through ThT fluorescence from the droplet after incubation.

To verify that the growth processes that we measure are not affected by preformed aggregates present in the original solution, we used size exclusion chromatography to purify the protein and to remove any such aggregates prior to carrying out the experiments; very similar data were obtained with and without size exclusion chromatography, and the propagation velocity is unaffected within experimental error (Fig. 2*B* and Fig. S1), indicating

that the observations do not originate from the presence of preformed aggregates.

The component amyloid structures within each microscale droplet are nanoscale and filamentous in nature. However, the fluorescence intensity fills homogeneously not only droplets of uniform diameter but also droplets with varying diameters (see Fig. 2B, *Inset* and Movie S4). The overall aggregation process cannot, therefore, result from the synchronized elongation of an ensemble of filaments; instead it must originate from nucleation and growth of a large number of individual fibrils. Thus, a single primary nucleation event must be able to trigger a cascade of spatially correlated subsequent events. Such a process requires secondary nucleation events, as many additional nucleation sites must emanate from the growing fibrils and promote further aggregation away from the initial primary nucleation site. The fibrils formed in this manner, therefore, themselves partake in subsequent conversion reactions, indicating that the overall process is a chain reaction where the products are also reactants for subsequent steps. Amyloid formation hence emerges as a process very different from normal gelation phenomena because, unlike in the latter process, primary nucleation events are rare and growth instead occurs through a molecular chain reaction.

Simple aggregation models, such as diffusion-limited aggregation schemes (29), have some analogies with the process that we observe and can also lead to a linearly growing gel. However, these models would not account for the fact that the fluorescence intensity at a given location in the droplets increases even after the initial wave has passed this location, as observed in our experiment (Fig. 2). Instead, therefore, we analyze the data here within the framework of reaction-diffusion phenomena (30) where the reaction continues even downstream of the reaction front. Within this framework, the time evolution of the local mass concentration of aggregates $M(\vec{r},t)$ is given as $\partial M(\vec{r},t)/\partial t = D\vec{\nabla}^2 M(\vec{r},t) + \kappa M(\vec{r},t)$, where D is the average diffusion coefficient of the aggregates (31). This description explicitly considers, through the reaction term proportional to κ, the secondary nucleation processes that are responsible for the chain reaction through the generation of new growth nuclei from existing aggregates. At the beginning of the reaction, we approximate κ as a constant, with a negligible decrease in the concentration of available soluble precursor proteins. In this approximation, the time evolution of the aggregate concentration can be evaluated in closed form: $M(\vec{r},t) = 2e^{\kappa t - \vec{r}^2/(4Dt)}/\sqrt{4\pi Dt}$, where the primary nucleation process occurs at $t = 0$. The behavior of the system is dominated by the exponential terms that dictate that the wave front propagates outward with a constant velocity $u = 2\sqrt{D\kappa}$, in accord with our experimental observations (Fig. 2). More generally, depletion of the monomers, which occurs as the aggregation process proceeds, requires the growth rate κ eventually to decrease to zero. This generalized form leads to the Fisher–Kolmogorov equation and a finite end value for $M(t)$; however, the velocity of the wave remains identical (30).

A reaction-diffusion process, as observed in a range of chemical systems, results in a propagating wave of constant velocity. An important additional prediction of this type of behavior is that the width of the reaction front also remains constant in time and, crucially, its value is connected to the ratio of the aggregate diffusion coefficient and the reaction rate: $w = \sqrt{D/\kappa} \log(2)$ (see *SI Text*). This prediction provides an important test to confirm the validity of the propagation mechanism. Measurements of the width of the front, as defined by the spatial extent over which the fluorescence intensity decays by a factor of 2, reveal that it is indeed constant in time as shown in Fig. 2C. This finding, therefore, provides strong support for the reaction-diffusion mechanism.

Using the measurements of the propagation velocity and width of the reaction front, we gain significant and unique insight into the microscopic events involved in the reaction-diffusion process.

By using the velocity and the width measurements, we can determine both the average diffusion coefficient of the aggregate species responsible for the propagation of amyloid growth and the corresponding rate constant; the values obtained are $D = (6.1 \pm 2.7) \cdot 10^{-13}$ m^2 s^{-1} and $\kappa = (2.0 \pm 0.9) \cdot 10^{-3}$ s^{-1}. The diffusion coefficient is approximately two orders of magnitude smaller than that of the monomeric protein (approximately 10^{-10} m^2 s^{-1}) and indicates that the species responsible for the propagation of the amyloid conversion reaction across space are relatively large diffusible aggregates, for which we can provide structural constraints through an estimate of the effective average hydrodynamic radius of 860 ± 380 nm. As the width of a typical amyloid fibril is approximately 10 nm the observed diffusion coefficient corresponds to an average fibril of length of *ca.* 10 μm, a value in excellent agreement with the lengths reported in a range of previous studies (32). These results indicate, therefore, that the propagation of amyloid growth is likely to take place through the diffusion of aggregated species.

Our data provide a striking visualization of the importance of secondary nucleation events in amyloid conversion and we have been able to show in this study that these events act to create traveling wave fronts that propagate the reaction not just in time but also in space. One compelling molecular model for the origin of secondary nucleation events (32), proposed on the basis of macroscopic measurements of amyloid growth, assumes that individual filaments grow through monomer addition and multiply in number through fragmentation (9, 10, 32), as shown in Fig. 3A. We can now extend this picture to include the spatial evolution of the growing amyloid filaments. To accomplish this objective, we perform Monte Carlo simulations of the spatial dynamics of a filament population evolving through filament elongation and fragmentation. The results reveal that the spatial patterns obtained in the simulations (Fig. 3) are remarkably similar to those measured in our experiments (Fig. 2) and confirm that a well-defined reaction front emerges even for the growth of a hetero-
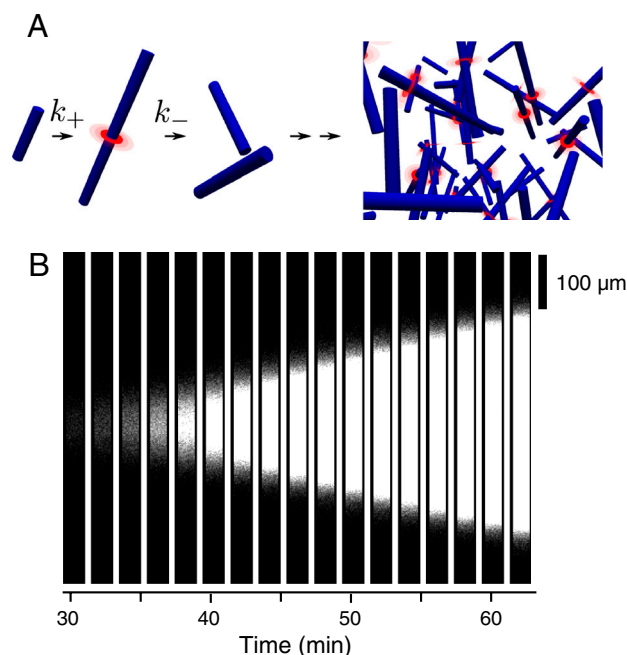

Fig. 3. Simulations of the spatial propagation of amyloid growth. The time evolution is computed starting from a single filament at $t = 0$ and followed by tracking the position and length of individual filaments as they grow (A) with an elongation rate $k_+ = 8.9 \cdot 10^4$ M^{-1} s^{-1} (see main text) in a monomer concentration of $m_{tot} = 5.2$ mM and multiply by fragmentation with a rate constant $k_- = 2.0 \cdot 10^{-8}$ s^{-1}. The amyloid conversion is observed to proceed as a chemical wave (B) in a markedly similar patter to that measured in the experiments (Fig. 2).

geneous population of aggregates. The only free parameters in the simulation are the microscopic rate constants for fragmentation k_- and elongation k_+; fixing the propagation velocity and the width of the reaction front to the experimentally measured values uniquely defines the microscopic rate constants to be $k_- = (2.0 \pm 0.5) \cdot 10^{-8}$ and $k_+ = (8.9 \pm 0.5) \cdot 10^4$ M^{-1} s^{-1}. These values are of the same order of magnitude as those obtained from previous bulk kinetic assays [$k_- = (1.7 \pm 1.3) \cdot 10^{-8}$ s^{-1} (33), $k_- = 2.1 \cdot 10^{-9}$ s^{-1} (10), $k_+ = (1.8 \pm 0.2) \cdot 10^5$ M^{-1} s^{-1} (33), and $k_+ = 2.9 \cdot 10^4$ M^{-1} s^{-1} (10)]. This result not only provides striking corroboration of the model (9, 32) but also reveals a unique role for fragmentation in defining the spatial evolution of growing amyloid filament systems.

A feature that is a marked characteristic of our data is the existence of a delay prior to the detection of amyloid formation by means of thioflavin T fluorescence in Fig. 2A and Fig. 4. The presence of such a lag phase is consistent with previous studies of amyloid growth kinetics in bulk solution and is typically attributed to the need for a primary nucleation process. The spatial propagation of amyloid growth revealed by our data suggests, however, that the average lag time $\langle \tau \rangle$ should depend on the system size. In our experiments, the process of amyloid fibril proliferation is defined by two distinct contributions to the lag time, one originating from the time required for a primary nucleus to form and the other from the time required for growth to generate detectable quantities of amyloid species as a result of the chain reaction associated with secondary nucleation. Crucially, the relative importance of these times is dependent on the volume in which the reaction is occurring. The primary nucleation time, $\langle \tau_n \rangle = c_n V^{-1}$, is governed by rare events characterized by a low primary nucleation rate, c_n, and therefore intrinsically depends on the system size, V. These events are likely to include a structural reorganization process that results in nuclei capable of further growth (34). By contrast, the growth time, τ_g, depends only on the efficiency of the chain reaction and is independent of system volume. Thus, for small system volumes $\tau_g \ll c_n V^{-1}$, and in this regime the lag time $\langle \tau \rangle \approx c_n V^{-1}$ is dominated by the primary nucleation time. By contrast, for large system volumes, $\tau_g \gg c_n V^{-1}$, and thus, in this second regime, the occurrence of primary nucleation events in the system becomes frequent; the lag time $\langle \tau \rangle \approx \tau_g$ is then primarily determined by the propagation time of the chain reaction. In general, therefore, the observed lag time is the sum of the two times, $\langle \tau \rangle = \langle \tau_n \rangle + \tau_g$, and the cross-over between these two regimes occurs when $\tau_g = \langle \tau_n \rangle$, yielding the corresponding volume $V_c = c_n \tau_g$. From this analysis, we can directly predict the sample size dependence of the lag time: $\langle \tau \rangle_V = c_n V^{-1} + \tau_g$.

Our use of microfluidic devices to confine the reaction volume in a microdroplet allows us to monitor this size dependent behavior directly, as we can measure independently both the primary nucleation and subsequent propagation steps while controlling the system size. The measured average lag time increases as the droplet size decreases as shown by the squares in Fig. 4A, in excellent agreement with the scaling behavior derived in the theory for $\langle \tau \rangle_V$, shown by the solid line in Fig. 4A. With increasing system size, however, this lag time does not tend to zero but rather approaches asymptotically a finite value. This value reflects the time required for the chain reaction to generate a sufficient quantity of fibrillar material for the Thioflavin T (ThT) fluorescence to be observable, $\tau_g = 93 \pm 8$ min. The nucleation-propagation mechanism implies, therefore, that a bulk system should exhibit this same lag time, and, in agreement with this prediction, a system 10^6 times larger than our largest drop size exhibits a lag time of 104 ± 19 min, close to this limit (Fig. 4).

Discussion

An important conclusion from the present analysis is that the measured lag time in bulk solution reflects growth through a chain reaction and is not, therefore, a measure of the time required for primary nucleation to occur. We can, however, use the fit in Fig. 4A to provide a direct measure of the primary nucleation rate per unit volume, $c_n^{-1} = 5.6 \pm 0.7 \cdot 10^6$ s^{-1} L^{-1}, under the conditions used in our study. A direct estimate of the time-scale associated with primary nucleation in a given droplet is therefore provided by subtracting the deterministic bulk lag time τ_g from the lag time measured in a given microdroplet. We also determine from the fit the characteristic volume where the behavior of the system changes from being limited by primary nucleation to being propagation limited, $V_c = C_n \tau_g = 31.8$ pL. For volumes that greatly exceed V_c, multiple nucleation sites should therefore be present. We can directly test this prediction by generating and studying droplets in the microfluidic system that are large enough to satisfy this condition (Fig. 4); strikingly, we visualize directly that amyloid growth in such systems is indeed propagated from multiple discrete nucleation sites (Fig. 4).

The limiting volume V_c represents a substantially smaller volume than those routinely accessible in bulk assays in vitro (mL–μL), but a volume larger than that of a typical living cell (fL–pL). This conclusion suggests that compartmentalization into and within cells, which is ubiquitous in biology and particularly in long lived organisms, offers a high degree of intrinsic protection, supported by extrinsic mechanisms such as molecular chaperones, against the uncontrolled aggregation of cellular proteins
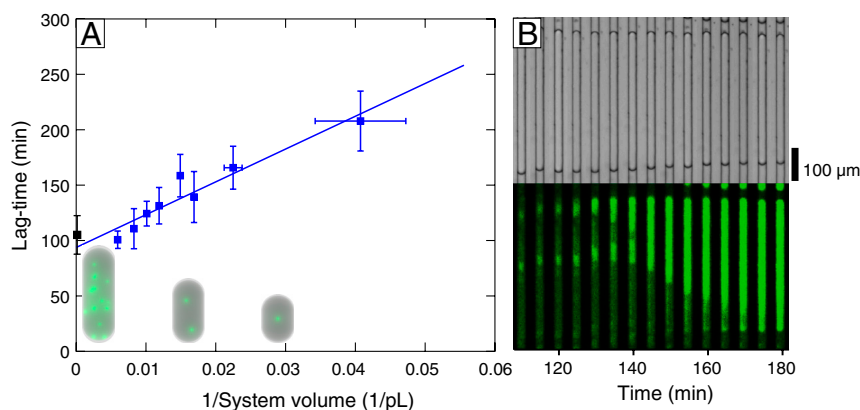
Fig. 4. Scaling of lag time with system size. In A, the lag times prior to the observation of fluorescence are reported for an array of 52 droplets of varying size measured simultaneously. A fit to the equation $\tau = c_n V^{-1} + \tau_g$ is shown in blue with $c_n = 1.7 \pm 0.25 \cdot 10^{-7}$ L^{-1} s and $\tau_g = 94 \pm 8$ min. The first data point (gray) shows the lag time in a macroscopic sample volume of 200 μL but otherwise identical conditions to the microfluidic data. The size independence in the limit of large systems originates from the presence of multiple nucleation sites for large volumes, as described in the text and schematically illustrated at the bottom of panel A. Multiple sites can be observed directly in droplets of sufficient size: panel B shows the time evolution of aggregation in such a droplet (Upper, bright field; Lower, fluorescence microscopy).

that can otherwise lead to pathogenic consequences. Such compartmentalization significantly enhances the kinetic stability of the soluble state of proteins in any given cell by decreasing very substantially the probability of primary nucleation relative to that in bulk solution, as illustrated by our data, and by limiting the diffusion of aggregates that are responsible for further proliferation as a consequence of secondary nucleation.

Finally, it is interesting to speculate that the exponential time dependence associated with chain reactions leads to very great sensitivity to the initial conditions and to potentially serious difficulties for controlling such processes should they occur in living systems. This factor may explain why evolutionary pressures appear to have overwhelmingly selected functional structures that assemble through a simple mechanism of primary nucleation (35) as the basis of multimolecular complexes, such as those involved in the cytoskeleton. Furthermore, in the small number of cases where amyloid growth has been found to be exploited by living systems for functional purposes, mechanisms have been observed to be in place to prevent the chain reaction associated with amyloid assembly from spreading, for example through the use of specific initiator elements to direct the polymerization reaction (36). The transmission of amyloid fibrils in space from one cell to another is increasingly appearing as a general characteristic feature of many situations where protein aggregation is implicated in vivo in the development of clinical disorders (37); our results provide a compelling mechanism for such spatial propagation through the action of diffusible aggregates.

In conclusion, by reducing the system size below a critical value using microfluidics, both primary and secondary nucleation events in amyloid formation can be observed and quantified independently. Moreover, this approach allows access to the spatial distribution of amyloid growth in solution, and reveals that the early stages of such growth display striking spatial inhomogeneities, a crucial characteristic absent in simpler gelation phenomena but essential to a fundamental understanding of amyloid growth and its potential consequences in vitro and in vivo.

Materials and Methods

Microfabrication. Microfluidic channels were fabricated into polydimethylsiloxane (PDMS; Dow Corning) using SU8 on silicon masters and standard soft lithography techniques (38, 39), and then plasma bonded to glass slides to create sealed devices. To minimize drying during the incubation period, glass coverslips were placed above the channels before curing the PDMS; this approach significantly reduces the volume of permeable PDMS in contact with the channels. Microdroplets were formed in an oil phase of Fluorinert FC-40 (Sigma–Aldrich) and 1.0% (w/w) PFPE-PEG block-copolymer surfactant (RainDance Technologies, Inc.). Syringe pumps (Harvard Apparatus) were used to control fluid flow.

Protein Solutions. The aqueous phase in each case contained 30 mg/mL bovine insulin in 50 mM HCl and 20 μM thioflavin T (all from Sigma–Aldrich). To check for the effects of preformed seed aggregates in the data showin in Fig. 2B, the protein solutions were purified by size exclusion chromatography. After centrifugation of a solution prepared in a volatile buffer (100 mM ammonium carbonate), the supernatant was injected and run on a superdex 75 26/60 column (GE Healthcare) using an Äkta prime FPLC system (GE Healthcare). The column was preequilibrated with 100 mM ammonium carbonate buffer before injection, and the peak fractions corresponding to the smallest molecular weight were collected, discarding the first and last fraction of the peak. The collected fractions were subsequently pooled and the concentration of the solution was measured by means of absorbance at 280 nm. The gel filtered solution was compared to the unfiltered solution by means of high resolution size exclusion chromatography (*SI Text*); the protein was dissolved in 10 mM HCl and 100 μL were run on a high resolution superdex 75 10/30 analytical size exclusion column (GE Healthcare) that had been equilibrated with 100 mM ammonium carbonate buffer. The chromatograms (Fig. S2) show an absence of aggregates in both solutions.

Reaction Front. The propagation velocity of the reaction front resulting from filament proliferation through growth and fragmentation was computed by considering the rate of production of filaments of a given length and their diffusion in space according to the Stokes–Einstein relation. The calculations were carried out using a custom C code (available on request). To facilitate comparison with the experiments, we use the geometric parameters for insulin filaments from (33) (filament diameter 6 nm, and filament length increment from monomer addition computed from the assumption of four monomers per cross-section of 4.8 Å).

1. Dobson CM (2003) Protein folding and misfolding. *Nature* 426:884–890.
2. Fowler DM, Koulov AV, Balch WE, Kelly JW (2007) Functional amyloid-from bacteria to humans. *Trends Biochem Sci* 32:217–224.
3. Sawaya MR, et al. (2007) Atomic structures of amyloid cross-beta spines reveal varied steric zippers. *Nature* 447:453–457.
4. Sacchettini JC, Kelly JW (2002) Therapeutic strategies for human amyloid diseases. *Nat Rev Drug Discov* 1:267–275.
5. Westermark P (2005) *Amyloid Proteins*, Amyloidosis and Amyloid Proteins: Brief History and Definitions (Wiley, Weinheim), 3.
6. Chiti F, Dobson CM (2006) Protein misfolding, functional amyloid, and human disease. *Annu Rev Biochem* 75:333–366.
7. Oosawa F, Asakura S (1975) *Thermodynamics of the Polymerization of Protein* (Academic, New York).
8. Xue W-F, Homans SW, Radford SE (2008) Systematic analysis of nucleation-dependent polymerization reveals new insights into the mechanism of amyloid self-assembly. *Proc Natl Acad Sci USA* 105:8926–8931.
9. Tanaka M, Collins SR, Toyama BH, Weissman JS (2006) The physical basis of how prion conformations determine strain phenotypes. *Nature* 442:585–589.
10. Knowles TPJ, et al. (2009) An analytical solution to the kinetics of breakable filament assembly. *Science* 326:1533–1537.
11. Ruschak AM, Miranker AD (2007) Fiber-dependent amyloid formation as catalysis of an existing reaction pathway. *Proc Natl Acad Sci USA* 104:12341–12346.
12. Ferrone FA, Hofrichter J, Sunshine HR, Eaton WA (1980) Kinetic studies on photolysis-induced gelation of sickle cell hemoglobin suggest a new mechanism. *Biophys J* 32:361–380.
13. Ferrone FA, Hofrichter J, Eaton WA (1985) Kinetics of sickle hemoglobin polymerization. II. A double nucleation mechanism. *J Mol Biol* 183:611–631.
14. Turnbull D (1952) Kinetics of solidification of supercooled liquid mercury droplets. *J Chem Phys* 20:411–424.
15. Li L, Ismagilov RF (2010) Protein crystallization using microfluidic technologies based on valves, droplets, and slipchip. *Annu Rev Biophys* 39:139–158.
16. Meier M, et al. (2009) Plug-based microfluidics with defined surface chemistry to miniaturize and control aggregation of amyloidogenic peptides. *Angew Chem Int Ed Engl* 48:1487–1489.
17. Whitesides GM (2006) The origins and the future of microfluidics. *Nature* 442:368–373.
18. Theberge AB, et al. (2010) Microdroplets in microfluidics: An evolving platform for discoveries in chemistry and biology. *Angew Chem Int Ed Engl* 49:5846–5868.
19. Waugh DF (1946) A fibrous modification of insulin. I. the heat precipitate of insulin. *JACS* 68:247–250.
20. Ivanova MI, Sievers SA, Sawaya MR, Wall JS, Eisenberg D (2009) Molecular basis for insulin fibril assembly. *Proc Natl Acad Sci USA* 106:18990–18995.
21. Jiménez JL, et al. (2002) The protofilament structure of insulin amyloid fibrils. *Proc Natl Acad Sci USA* 99:9196–9201.
22. Knowles TPJ, et al. (2007) Kinetics and thermodynamics of amyloid formation from direct measurements of fluctuations in fibril mass. *Proc Natl Acad Sci USA* 104:10016–10021.
23. Brange J, Langkjoer L (1993) Insulin structure and stability. *Pharm Biotechnol* 5:315–350.
24. Dische FE, et al. (1988) Insulin as an amyloid-fibril protein at sites of repeated insulin injections in a diabetic patient. *Diabetologia* 31:158–161.
25. Aguzzi A, Haass C (2003) Games played by rogue proteins in prion disorders and Alzheimer's disease. *Science* 302:814–818.
26. Schmitz CHJ, Rowat AC, Kster S, Weitz DA (2009) Dropspots: A picoliter array in a microfluidic device. *Lab Chip* 9:44–49.
27. Holtze C, et al. (2008) Biocompatible surfactants for water-in-fluorocarbon emulsions. *Lab Chip* 8:1632–1639.
28. Sigurdson CJ, et al. (2007) Prion strain discrimination using luminescent conjugated polymers. *Nat Methods* 4:1023–1030.
29. Weitz DA, Huang JS, Lin MY, Sung J (1984) Dynamics of diffusion-limited kinetic aggregation. *Phys Rev Lett* 53:1657.
30. Grindrod P (1996) *The Theory and Applications of Reaction-Diffusion Equations* (Oxford University Press, London).

31. Ferrone F (1999) Analysis of protein aggregation kinetics. *Methods Enzymol* 309:256–274.
32. Collins SR, Douglass A, Vale RD, Weissman JS (2004) Mechanism of prion propagation: Amyloid growth occurs by monomer addition. *PLoS Biol* 2:e321.
33. Smith JF, Knowles TPJ, Dobson CM, Macphee CE, Welland ME (2006) Characterization of the nanoscale properties of individual amyloid fibrils. *Proc Natl Acad Sci USA* 103:15806–15811.
34. Auer S, Meersman F, Dobson CM, Vendruscolo M (2008) A generic mechanism of emergence of amyloid protofilaments from disordered oligomeric aggregates. *PLoS Comput Biol* 4:e1000222.
35. Alberts B, et al. (2002) *Molecular Biology of the Cell* (Garland, New York), 4th Ed.
36. Chapman MR, et al. (2002) Role of Escherichia coli curli operons in directing amyloid fiber formation. *Science* 295:851–855.
37. Aguzzi A, Rajendran L (2009) The transcellular spread of cytosolic amyloids, prions, and prionoids. *Neuron* 64:783–790.
38. Qin D, Xia Y, Whitesides GM (2010) Soft lithography for micro- and nanoscale patterning. *Nat Protoc* 5:491–502.
39. Xia Y, Whitesides GM (1998) Soft lithography. *Annu Rev Mater Sci* 28:153–184.

APPLIED PHYSICAL
SCIENCES